


# Landslide Mapping Using Two Main Deep-Learning Convolution Neural Network Streams Combined by the Dempster–Shafer Model

Omid Ghorbanzadeh , Sansar Raj Meena, Hejar Shahabi Sorman Abadi , Sepideh Tavakkoli Piralilou, Lv Zhiyong , and Thomas Blaschke 

**Abstract**—Beyond the direct hazards of earthquakes, the deposited mass of earthquake-induced landslide (EQIL) in the riverbeds causes the river to thrust upward. The EQIL inventories are generated mostly by the traditional or semisupervised mapping approaches, which required a parameter’s tuning or binary threshold decision in the practical application. In this study, we investigated the impact of optical data from the PlanetScope sensor and topographic factors from the ALOS sensor on EQIL mapping using a deep-learning convolution neural network (CNN). Thus, six training datasets were prepared and used to evaluate the performance of the CNN model using only optical data and using these data along with each and all topographic factors across the west coast of the Trishuli river in Nepal. For the first time, the Dempster–Shafer (D–S) model was applied for combining the resulting maps from each CNN stream that trained with different datasets. Finally, seven different resulting maps were compared against a detailed and accurate inventory of landslide polygons by a mean intersection-over-union (mIOU). Our results confirm that using the training dataset of the spectral information along with the topographic factor of the slope is helpful to distinguish the landslide bodies from other similar features, such as barren lands, and consequently increases the mapping accuracy. The improvement of the mIOU was a range from approximately zero to more than 17%. Moreover, the D–S model can be considered as an optimizer method to combine the results from different scenarios.

**Index Terms**—Earthquake-induced landslide (EQIL), hydropower, landslide-induced lakes, topographical factors, Trishuli river.

Manuscript received June 30, 2020; revised July 22, 2020, August 10, 2020, and October 24, 2020; accepted December 3, 2020. Date of publication December 10, 2020; date of current version January 6, 2021. This work was supported in part by the Austrian Science Fund (FWF) through the Doctoral College GIScience under Grant DK W 1237-N23 at the University of Salzburg. (Corresponding author: Omid Ghorbanzadeh.)

Omid Ghorbanzadeh, Sepideh Tavakkoli Piralilou, and Thomas Blaschke are with the Z\_GIS Centre for Geoinformatics, University of Salzburg, 5020 Salzburg, Austria (e-mail: [omid.ghorbanzadeh@stud.sbg.ac.at](mailto:omid.ghorbanzadeh@stud.sbg.ac.at); [sepideh.tavakkoli-piralilou@stud.sbg.ac.at](mailto:sepideh.tavakkoli-piralilou@stud.sbg.ac.at); [thomas.blaschke@sbg.ac.at](mailto:thomas.blaschke@sbg.ac.at)).

Sansar Raj Meena is with the Department of Geoinformatics, University of Salzburg, 5050 Salzburg, Austria (e-mail: [sansarraj.meena@sbg.ac.at](mailto:sansarraj.meena@sbg.ac.at)).

Hejar Shahabi Sorman Abadi is with the Remote Sensing and GIS, University of Tabriz, Tabriz 5166616471, Iran (e-mail: [hejarshahabi@gmail.com](mailto:hejarshahabi@gmail.com)).

Lv Zhiyong is with the School of Computer Science and Engineering, Xi’an University of Technology, Xi’an 710048, China (e-mail: [lvzhiyong\\_fly@hotmail.com](mailto:lvzhiyong_fly@hotmail.com)).

Digital Object Identifier 10.1109/JSTARS.2020.3043836

## I. INTRODUCTION

THE loss of property and human life due to earthquake-triggered landslides are significantly high, and due to climate change, it will certainly rise [1]. Almost 70% of casualties related to the earthquake are not caused by the shaking of the ground instead of affected by landslides [2]. About 47 000 earthquake-induced landslides (EQILs) casualties were reported from 2004 to 2010 [3]. The EQIL has direct and indirect long-term socioeconomic effects on the society along with the environmental effects [4]. There are some direct damages of an earthquake, such as blocking of rural and main roads, damaging bridges, settlements, and especially the hydroelectric projects that are considered as one of the main energy supply for the local population [5], [6]. However, there are some indirect consequences, such as the failure of landslide-induced dams, which lead to catastrophic floods in the downstream areas [7]–[9], which is again harmful to several mentioned public and private infrastructures.

The EQIL and its adverse consequence of landslide dams are considered to be a significant natural hazard in the mountain regions of the Himalayas [10], [11]. Although landslides mostly occur in remote areas, the resulting catastrophic flash floods are the reason for extensive damage to the downstream regions of the river in this area. Along with the severe threats to the environment, these floods have a long-term economic impact on an area of settlements, hydroelectric projects, and agriculture fields in the downstream areas.

Therefore, there is a growing demand for making EQIL inventories and we have still inadequate information on the landslide occurrence across the drainage networks. This uncertainty in the landslide inventory production affects the further hazard and risk analysis [12]. All landslide susceptibility modeling and mapping approaches are based on an accurate inventory dataset. This inventory dataset is usually used for training the hazard models to find the potential landslide-prone areas [13], [14].

Moreover, this inventory dataset is crucial for the evaluation and accuracy assessment processes of the resulting hazard maps [15], [16]. Consequently, imprecise potential landslide-prone areas may result in driving the wrong risk modeling and mapping [17]. Several studies have analyzed hazard mitigation strategies and the application of landslide risk potential mapping is increasing [18]. The reliability of such studies is strongly dependent

on the accurate and complete inventory datasets of past hazard events, to make spatial predictions for future events [19], [20].

To achieve the hazard potential assessment and risk mapping, there is very limited information related to EQIL, and the main reason for having limited access to landslides information is the remoteness of most of the mountainous regions that make it difficult and, in some cases, impossible to conduct field surveys [21]. Therefore, remote sensing (RS) data are considered as the main source of getting information about the impacts of a natural hazard on the environment [22]. Different studies have used various geodatabases, including different RS products optical data and topographical information for the landslide detection.

In recent years, the RS data, including very high-resolution (VHR) images, are widely applied for the EQIL detection and mapping using multiple methodologies, including machine learning (ML) models [23]. Mezaal *et al.* [24] applied the object-based landslide detection using different ML models of support vector machines (SVM), K-nearest neighbor, and random forest (RF). Danneels *et al.* [25] used an artificial neural network (ANN) as an automatic landslide detection methodology by multispectral advanced spaceborne thermal emission and reflection radiometer images. An unsupervised feature learning method of a stochastic neural network of the restricted Boltzmann machine was applied by Zhu *et al.* [26] for landslide susceptibility assessment. Martha *et al.* [27] used spectral information together with morphometric characteristics and shape to separate landslides from nonlandslide areas. Hölbling *et al.* [28] also used object-based environment spectral, spatial, and morphological properties as well as context information for the landslide detection.

During the last decade, deep-learning models, other ML methods, and CNNs have been applied successfully in broad range object detection aims [29]. A deep belief network along with a logistic regression classifier was used by Ye *et al.* [30] to detect landslides on hyperspectral images. Guirado *et al.* [31] and Lv *et al.* [32] used freely available high-resolution Google Earth images for the scattered shrub detection with a CNN model. Ghorbanzadeh *et al.* [33] and Quinn *et al.* [34] applied the CNN model for dwelling detection in refugee camps from VHR imagery sources, including worldview imagery (0.3–0.5 m) in different studies. Although CNN models have acquired surprising results for some object annotation from the aerial images, a limited number of studies exist that use the CNN model for the EQIL detection. Ghorbanzadeh *et al.* [12] evaluated the performance of different CNN models for landslide detection and compared it with those of three different ML models, namely, ANN, SVM, and RF. A comprehensive meta-analysis and systematic review for the RS image classification by Sheykhmousa *et al.* [35]. A four layers CNN model was structured and used by Lu *et al.* [36] for the soil detection.

The literature review shows that the potential of CNN models for the EQIL mapping has not been fully explored yet. Furthermore, our study can be considered as one of the first studies using the CNN model for the detection of EQILs considering the impact of topographical factors. The impact of every applied topographical factor is assessed using the Dempster–Shafer (D–S) model. The fusion of different spatial data with the D–S

model, as well as its application in the landslide detection and susceptibility modeling, has been presented and fully described by Piralilou *et al.* [13], Nachappa *et al.* [20], and Althuwaynee *et al.* [37], respectively. However, the capability of this model for combining the results of different CNN streams is still unclear. Moreover, we want to introduce an optimized EQIL map by combining the resulting maps from each training dataset of the spectral information along with every single topographic factor. Therefore, we do not rely only on the data fusion within the CNN but the probability model of D–S is used to enhance the mapping. The applied CNN structure in this study is designed and trained in Trimble’s eCognition software based on the Google TensorFlow software library and the D–S model is done within the QGIS environment.

In the remainder of this article, we compare the CNN results generated from different training datasets with a precise EQIL inventory of polygons using the mean intersection-over-union (mIOU) validation method.

Our study can be considered as the first study that lies in evaluating the impact of topographic factors for EQILs detection using convolutional neural networks (CNNs). In this regard, we present the RS approach based on the optical satellite imagery from the PlanetScope sensor and topographical factors prepared from a 5 m resolution digital elevation model (DEM) acquired from the Japanese aerospace exploration agency JAXA ALOS sensor to detect the EQILs using the CNN model.

## II. STUDY AREA

The study area is located in the higher Himalayas and is one of the most landslide-prone regions along the Trishuli river in the Rasuwa district in Nepal (see Fig. 1).

In the summer of 2015 after the Gorkha earthquake, more than 80 people were killed due to EQILs and flood events near the Mailung village hydropower plant camps. The damages led to a decline in energy production and high economic losses (Schwanghart *et al.* [38], 2018). Therefore, the landslide susceptibility and risk mapping in the upstream areas of the river is an essential requirement for securing hydroelectric project sites and consequently, the local energy supply. Forest is the predominant land cover, followed by grassland, shrubland, agriculture, and rural habituated areas. The climate of this region is under the influence of the orographic monsoon precipitation with the annual average rainfall of 691 mm. EQIL dammed the river that leads to the occurrence of some lakes behind the dams in several locations. Water blockage behind the landslides induced dams is the main reason for the catastrophic flash floods along with the monsoonal rains. The flash floods of this river caused damage to the hydropower project sites that are present in the study area.

## III. MATERIALS AND METHODS

### A. Inventory Records

In this study, an inventory dataset of the polygons of the landslides for the study area was prepared from a manual delineation of landslides based on the PlanetScope imagery. We used

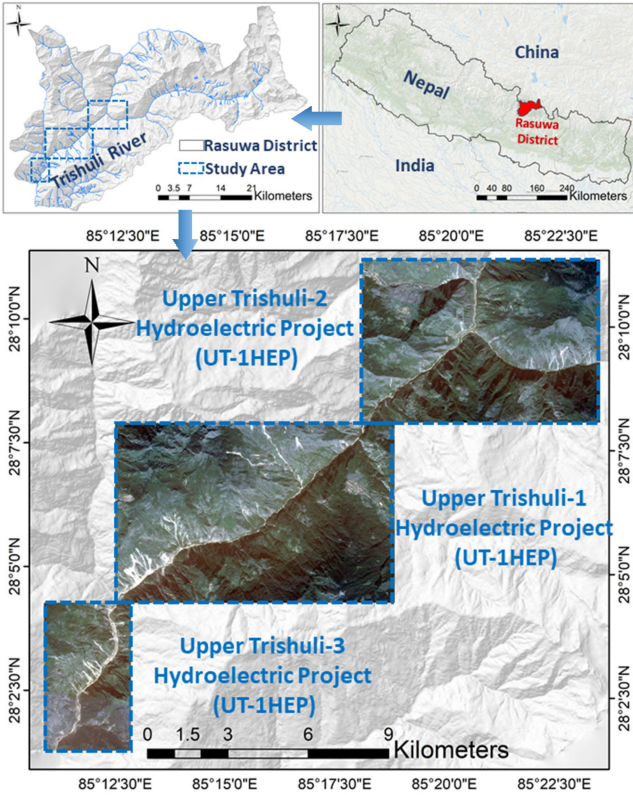


Fig. 1. Geographic location of the study area illustrated by a true color composite of PlanetScope bands 3/2/1 acquired on 28 November 2015.

cloud-free planet scope imagery from November 2019 to digitize landslides using the visual image interpretation manually. A total number of 168 landslide events were mapped as polygons, which cover an area of 326.59 hectares. The prepared landslide inventory dataset was then visually verified using the available field data of GPS points of the landslide.

### B. Satellite Imagery

The satellite images are taken from the Planet Labs, Inc. PlanetScope that includes about 120 dove satellites, which provide 3-m spatial resolution images in four-band multispectral [blue (455–515 nm), green (500–590 nm), red (590–670 nm), and NIR (780–860 nm)] [39]. Landslides often have the same spectral response to their surrounding environment [40]. The analysis of the multispectral data in the study by Fayne *et al.* [41] suggested that increases in the red wavelength band enable the detection of the spectral characteristics of landslides and barren areas in hilly terrain and forested areas. The optical band of single red, green, and blue (RGB) is useful for the identification of landslides areas in the imagery but it is not sufficient to differentiate between vegetation growths in a shadow region. In that case, the additional band of infrared enables preventing the drawbacks of the mixed spectral response of landslides to only RGB spectral data. The PlanetScope four spectral bands were used for calculating the normalized difference vegetation index (NDVI) [see (1)] as the basis for the landslide detection. The NDVI represents the surface reflectance and gives the estimate

of vegetation growth or loss in the study area, which may affect the landslide occurrence.

$$\text{NDVI} = \frac{(\text{NIR} - \text{Red})}{(\text{NIR} + \text{Red})}. \quad (1)$$

### C. Topographical Factors

The physical and environmental conditions of a region affect the landslide occurrence [42], [43]. Based on the previous studies in the study area and extensive literature review as well as the field survey point out that the topographical factors selected in this study are well associated with the distribution of landslide occurrence and their spatial distribution [12]. Also, the selection of landslide detection data depends on the local terrain conditions and their relation to the physiographical features of the study area [44]. The occurrence of landslides is highly dependent on the surface topography [37] and most of the study area consists of hilly terrain. Topographical information was extracted from a DEM 12.5 m from the ALOS PALSAR sensor (see Fig. 2).

1) *Elevation*: Elevation affects the topographical attributes and earth surface morphology, which influences the spatial variability of precipitation, vegetation, soil thickness, and credibility of the rock mass [45]. In a study related to EQIL by Fan *et al.* [46] shows that coseismic landslides frequently occur at higher elevations as they are influenced by the gravity.

2) *Slope*: The slope is crucial because the sliding of a mass of the earth is directly linked to the slope steepness. The slope angle can represent the steepness of terrain and the slopes with high steepness are prone to landslide occurrence. On the other hand, low-angle slopes are more prone to the activity of channelized deposits, which results in fall and debris slides [46].

3) *Aspect*: The slope aspect is essential because the slope with different orientation experiences different solar radiation and precipitation, which can influence the slope stability [47]. The slope aspect is classified into eight classes representing geographical directions and an additional class represents the flat surface. The slope aspect influences the spatial distribution of landslide occurrence as it impacts the infiltrating properties, permeability, and pore water pressure of the surface.

4) *Plan Curvature*: The plan curvature reflects the topography and the complexity of the terrain. The convergence and divergence of water downslope are influenced by the plan curvature. When the flow of water increases down the slope, it leads to a considerable amount of erosion, which leads to the instability of the slope. The positive values of plan curvature represent the convexity of the slope, the negative values represent the concavity, and the null value shows the linear or flat surface.

### D. Convolution Neural Network

Deep learning (DL) is based on ANN and considered as a subset of ML, including techniques that mimic how our brain works. DL is largely based on ANN with several hidden layers that require a considerable amount of data to train, so to get better performance [31], [48]. The flowchart of the whole applied methodology is represented in Fig. 3.

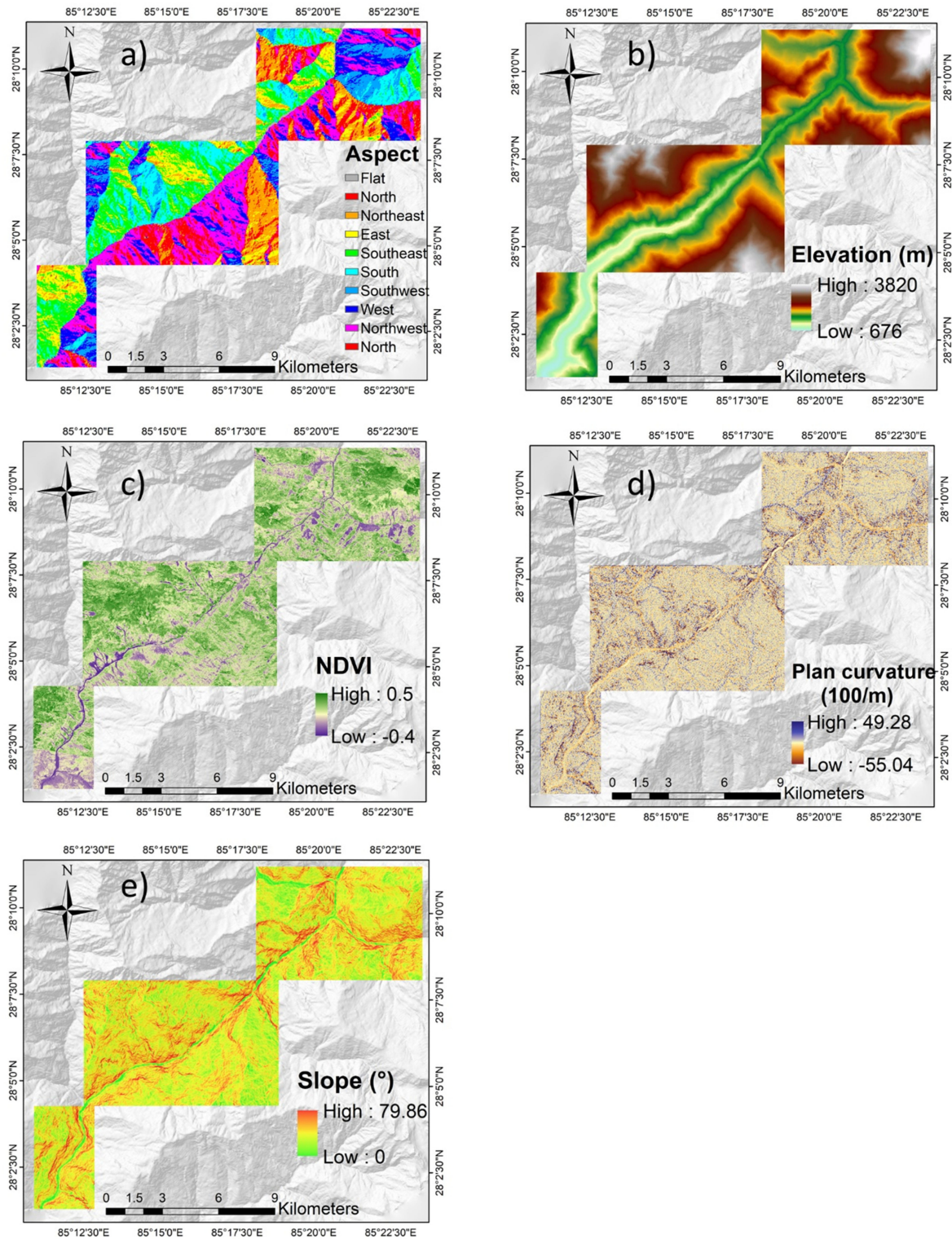


Fig. 2. Layer of conditioning factors. (a) Slope aspect. (b) Altitude. (c) NDVI. (d) Plan curvature. (e) Slope.

We use a type of DL in this study called CNN. One of the advantages of using the CNN model is that it can learn useful feature representations of an image with no need to design the low-level ones manually. However, this matter makes it hard to explain what it exactly learns [49]. The CNN model has a specific architecture and contains convolutional and pooling

layers, whereby the convolutional layer is the primary building block of any CNN model. In any neural network, all neurons existing in the layer  $n$  are acting as the inputs to layer  $n+1$  neurons, while in a CNN model, the neurons of layer  $(n+1)$  are not fully connected to all neurons of layer  $n$  but only connected to a corresponding subset of them, which is called the receptive

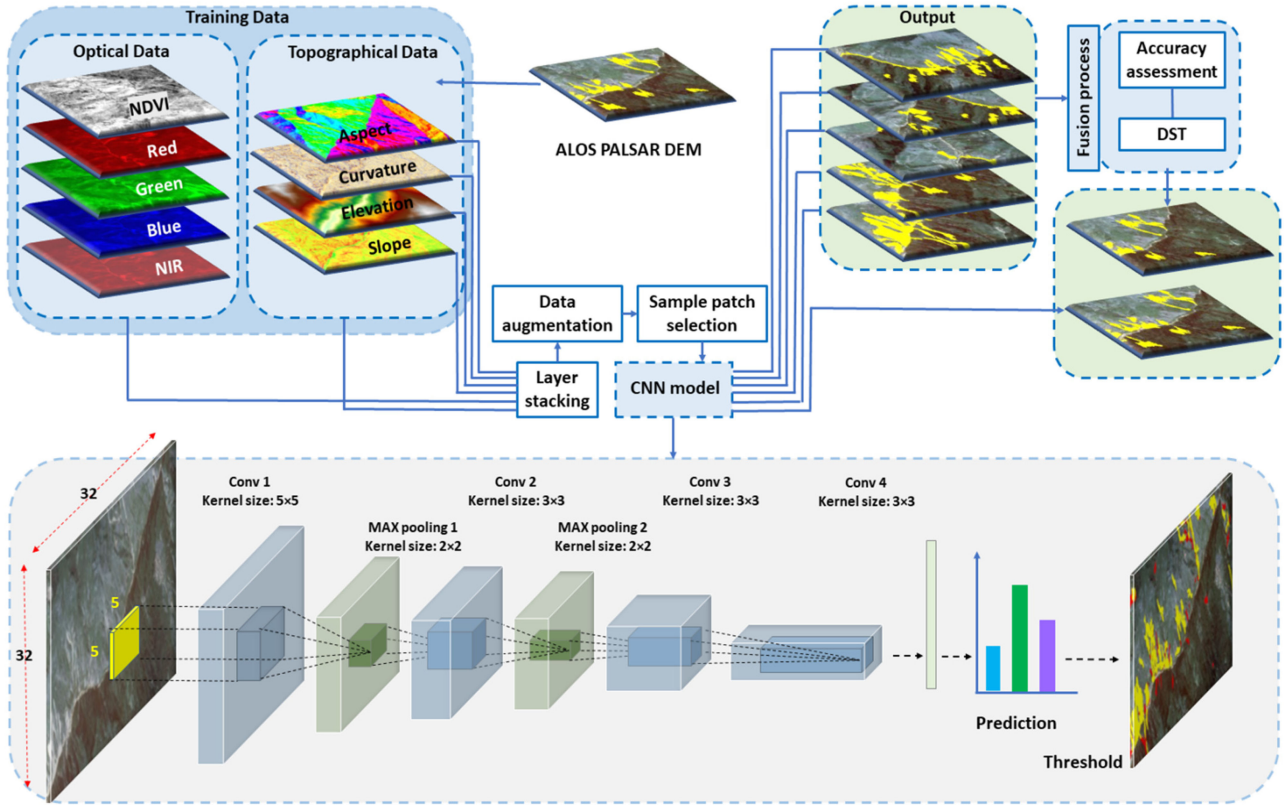


Fig. 3. Applied CNN model architecture trained separately with two different training datasets.

field. The reason behind that is feedforwarding an image of  $32 \times 32$  as an input, the first layer will require 1024 neural nodes and also much more nodes within the next hidden layers. Moreover, the fully connected networks make the model more complicated with more number of weight parameters, which is expensive to run and hinder the training process [50]. To deal with this problem, the conventional neural networks with the local connection among layers were introduced by LeCun and Bengio [51]. The local connections among layers turned the DLs into one of the most popular models in the image classification. Several articles provided comprehensive descriptions of the structure of CNN models and the way that they used to handle training and testing processes [47], [52].

In our case, the first convolution layer was used with a kernel size of five and continued with three convolution layers with a kernel size of three. The pooling layer is used to down/subsample the output of the convolutional layer to produce a concise set of feature maps that leads to a reduction of the computation volume for the reminder layers. In the CNN model of this study, three max-pooling layers of  $2 \times 2$  were applied.

Our CNN model was fed once with a five-layer training dataset, including the optical data of spectral bands and the NDVI (we call it  $CNN_O$ ). Then we added topographic factor layers, namely, slope, aspect, plan curvature, and altitude to the previous dataset, to train our  $CNN_{OT}$  model. In this case, the optical data (spectral bands) along with the topographic factor layers fed to the  $CNN_{OT}$ , where  $T$  refers to the applied

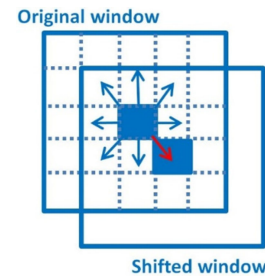


Fig. 4. Random window shifting technique.

topographic factor layers for training the model. Therefore, we use two main CNN models of  $CNN_O$  and  $CNN_{OT}$ .

#### E. Data Augmentation

The CNN model needs a considerable amount of data for efficient training, and the size of the training dataset can considerably affect the results of the CNN model. In the present study, due to the different sizes, shapes, and directions of the EQILs, we applied a random original window shifting technique (see Fig. 4). In this regard, the central point of the sample window was shifted randomly within a small buffer, and consequently, the window itself was shifted and covered other areas in the sample.

Using this augmentation technique for both our training, the datasets increase the size of them about two times.

### F. Application of D-S Model

The concept of the D-S model is introduced by Dempster [53], which is based on the Bayesian probability theory [54]. It is considered a practical approach to integrate the spatial data with mathematical representation to deal with the associated uncertainty in mapping and modeling approaches [55]. Within a set of mutually exclusive hypotheses, which is called the frame of discernment, more evidence can be considered [56]. The D-S model is a converted form of events to the proposition and an event set to the proposition set, which defines the concept of the function  $m$  known as the basic probability assignments function, degree of belief of the element  $A$  from event set called  $\text{Bel}(A)$ , and the degree of plausibility (or verisimilitude) of the element  $A$  shown as  $\text{Pl}(A)$ . The functions of  $\text{Bel}$  and  $\text{Pl}$  show the value of the lower and upper bound for an unknown probability function. The difference between these two functions indicates the associated uncertainty.

For the case of spatial data integration, the D-S model delivers a framework for evaluating the associated uncertainty of mapping and modeling approaches with an uncertain event of the probability  $P(M_l)$  that another result  $M_l$ ,  $l = 1, \dots, n$  is correct. Therefore, the lower bound shows the degree of belief that indicates  $M_l$  is correct and refers to  $\text{Bel}(M_l)$ , while the upper bound shows the probability of  $M_l$  as the plausibility  $\text{Pl}(M_l)$  [57] as follows:

$$\text{Bel}(A) = \sum_{B \subseteq A} m(B) \quad (2)$$

$$\text{Pl}(A) = \sum_{B \cap A \neq \emptyset} m(B) \quad (3)$$

where  $\text{Bel}(A)$  is the minimum belief in hypothesis  $A$  and the  $\text{Pl}(A)$  refers to the maximum belief in hypothesis  $A$ . Therefore, the resulting interval of  $[\text{Bel}(A), \text{Pl}(A)]$  that  $\text{Bel}(A) \leq \text{Pl}(A)$  is considered as a measure to show the associated uncertainty within set  $A$  [58]. Unlike the probabilistic model that assigns a mass to the individual elementary events, the D-S model makes  $m(A)$  on the set  $A$  of the  $P(z)$ , power sets of the space  $Z$  event. Thus,  $m(A)$  states the degree of belief that the element of  $x$  goes to the set  $A$  itself and not its subsets [13], [59]. The basic probability assignments that give a mass in the interval of  $[0, 1]$  every subset of set  $A$  is based on the following:

$$m : P(z) \rightarrow [0, 1], m(\emptyset) = 0; \sum_{A \in Z} m(A) = 1. \quad (4)$$

If we have  $n$  data sources, the probability masses of  $m_i(B_j)$  should be specified for every data source  $i$  with  $1 \leq i \leq n$  and for all sets,  $B_j \in 2^\theta$ . The D-S MODEL allows the combination of these probability masses from the results of each approach and the applied inventory dataset to represent an integrated probability mass for each set [20]. The composition rule in the D-S model is the basis of the integrating of mass functions  $m_i$  found from  $n$  different sources of data given in the following equations:

$$m(A) = m_1(B_1) m_2(B_2) m_3(B_3) \dots m_n(B_n) \quad (5)$$

$$m(A) = \frac{\sum_{B_1 \cap B_2 \dots B_n = A} \prod_{i=1}^n m_i(B_j)}{(1 - K)} \quad (6)$$

where  $K$  denotes the degree of conflict given as

$$K = \sum_{B_1 \cap B_2 \dots B_n = \emptyset} \prod_{i=1}^n m_i(B_j). \quad (7)$$

For further explanation of the D-S model and the mathematical formulation, refer to [55] and [60]. In the present study, the CNN model was trained based on the optical data and then each topographic factor of the slope angle, slope aspect, plan curvature, and altitude was added to the optical data as auxiliary information to the EQIL detection. Based on considering different training datasets, different landslide detection maps were generated and grouped by the fusion level analysis technique [24]. This technique sets different classified pixels together and fuses them into the desirable class according to the belief confusion matrix [61]. Thus, the resulting EQIL detections based on each training datasets were combined by fusing the D-S model with the inventory dataset that is used for training the CNN. The D-S model used the fused class label of the EQIL or non-EQIL represented by any single pixel in the maximal belief function. The definition of the precision accuracy assessment metric is used for the estimation of the belief functions for the classification results. A confusion matrix is used for this aim, which fuses the highest probability of a class.

## IV. RESULTS AND VALIDATION

First CNN was trained with five spectral layers from the PlanetScope imagery (R, G, B, NIR, and NDVI). Besides, we created five additional topographical layers, i.e., slope, aspect, plan curvature, and altitude. The EQIL distribution in each class of the applied conditioning factors for training the CNN model is represented in Fig. 5. The described architecture of the CNN model was trained with six training datasets from outside of the study site. Then the trained model was tested in the study site of the hydroelectric project. The detected polygons as the landslide, which were smaller than  $350 \text{ m}^2$ , were ignored regarding reducing the false-negative (FN) results. The optimal thresholds of more than 90% were used to select the most appropriate landslide detection within cross validation for all resulting CNN-based probability maps. The D-S model was used to combine all resulting maps from different applied scenarios. The resulting maps are presented in Fig. 6.

We outline four accuracy assessment methods, which are widely used in computer vision and object detection. The accuracy assessment process was used to evaluate the effectiveness and performance of the applied CNN model using different training datasets comparing with that of the D-S model. The quantitative accuracy assessment measures of precision (8), recall (9), and  $F1$ -score (10) [62] were used to assess the accuracy of the resulting EQIL detections. The results were compared with the inventory landslide dataset, which was reserved for result validation and was not used for the training process. Precision measures how each training dataset could detect the landslides and recall refers to how many landslides are correctly detected. The accuracy assessment measure of  $F1$ -score is a combination element between precision and recall [63]. The mIOU is another accuracy assessment measure used to evaluate the accuracy of the EQIL detection results. The mIOU is used

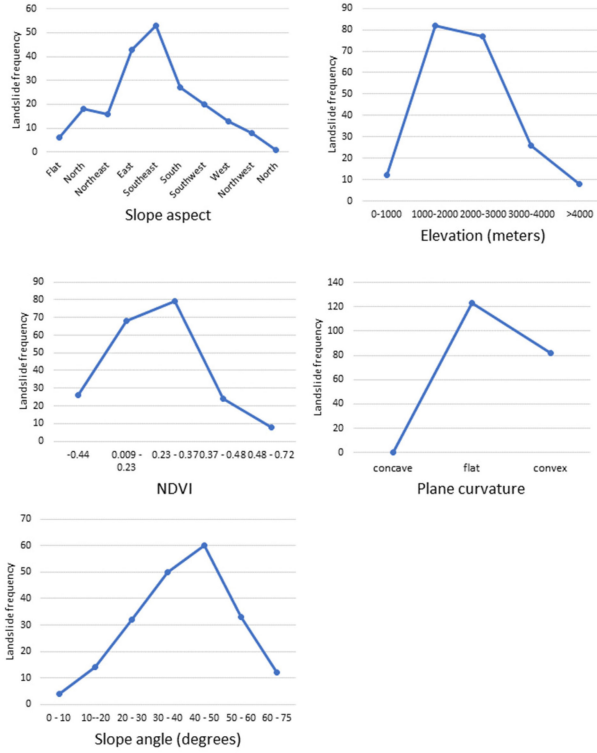


Fig. 5. Landslide distribution in each topographic factor.

by Ghorbanzadeh *et al.* [12] to validate the results of landslide detection based on different ML models and DL approaches. This validation measure is extensively used in the image processing and computer vision for object detection cases [64]. The mIOU (11) is an appropriate measure to validate the results that are in polygon based on an inventory dataset of which is also represented by polygons [see Fig. 7 and (5)].

All applied accuracy assessment measures were calculated based on three metrics, namely, FNs, true positives (TPs), and false positives (FPs). The FNs indicate the EQILs that are not detected. The TPs are correctly identified landslides and the FPs metric refers to misdetections (see Table I). The results of each single accuracy assessment measure for every landslide detection approach are represented in Table II

$$\text{Precision} = \frac{\text{TP}}{\text{TP} + \text{FP}} \quad (8)$$

$$\text{Recall} = \frac{\text{TP}}{\text{TP} + \text{FN}} \quad (9)$$

$$F1 = 2 \times \frac{\text{Precision} \times \text{Recall}}{\text{Precision} + \text{Recall}} \quad (10)$$

$$\text{IOU} = \frac{\text{Area of Overlap}}{\text{Area of Union}}. \quad (11)$$

## V. DISCUSSION

Extracting and detecting the exact border of EQIL to avoid their threats to the riverbeds and the hydroelectric projects in

the mountain regions of the Himalayas is an important task (see Fig. 9). Therefore, it is essential to evaluate the impact of the condition factors on the detection of the EQILs. The present study proves that it is essential to select the appropriate training factors for landslide detection within a CNN model. The results of our study showed that using some of the topographical layers as part of the CNN model, the training dataset somewhat reduced the accuracy of EQIL mapping in our study site. This lower accuracy is mainly due to most of these factors cannot specify the landslide area with the neighboring areas in landslide detection [12]. However, this matter is entirely vice versa regarding using these factors for the landslide susceptibility mapping as it has been proved in several published articles in this field. For example, aspect information can show the higher frequency of the landslide events that happened in a specific aspect (e.g., northeast) in a study area. While if the CNN trained that the northeast aspect has a higher probability of the landslide event, it might increase FPs and FNs in areas in this aspect where it has spectral similarities with a landslide. We used different additional layers as auxiliary topographical input information to help our model to distinguish between riverbeds, the built-up areas, and the landslides, which have spectral similarities but usually have different topography. The CNN model, which was trained with data, including the slope layer, performed better (0.72 *F*-score) than when we added other topographical layers, including aspect, curvature, and DEM to the optical data. Although for the case that was trained with the auxiliary data of the DEM layer, the *F*-score was the lowest value of 0.58, this layer could successfully separate riverbeds from the landslides. However, the huge amount of FPs (343.81 ha) mostly in the higher elevations did not let this scenario get a high *F*-score, while the curvature layer was useful to carefully detect the landslides in the higher elevations. Nevertheless, the riverbed was the main challenge for the model trained by adding the curvature layer. As most of the landslide in our case study area happened in the south and southeast of the valley, the trained model with the aspect layer could not properly detect the landslides happened in the other aspects, such as the north aspect (see Fig. 8).

The lowest TPs of 273.01 ha were resulted by using all of the topographic factors for training the CNN model. However, using only the optical data led to the highest TPs of 322.39. The topographic factors are always considered as the main conditioning factors for landslide modeling. However, these factors were not generally helpful to the detection of this natural hazard using our applied CNN model. Nevertheless, adding the slope data as auxiliary information was very practical for separating the landslide areas from the riverbed (see Fig. 8) as the slope angle within the riverbeds is usually a value close to zero, unlike the EQIL areas. Moreover, spectral information, especially NDVI was cooperative for detecting the exact border of EQIL along with the whole landslide. The reduction of the accuracy using topographical factors can be described as most of the landslides are located in steep areas along the river; the CNN model overestimates landslides in these areas. We may say that, in the present study, using the topographical information did not improve the landslide detection results. Nevertheless, it is not

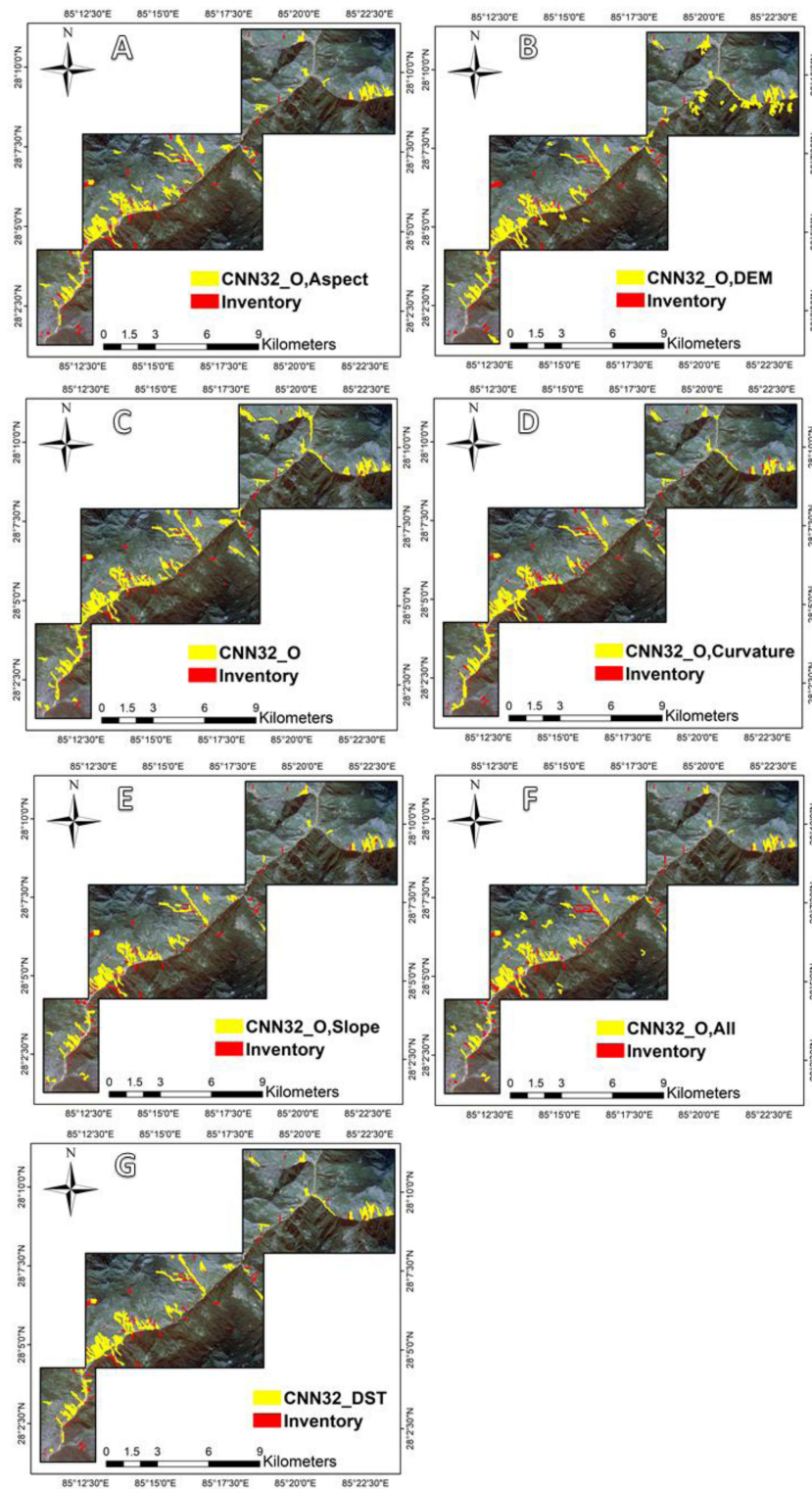


Fig. 6. Landslide detection results.

as simple as to generally concluding such that since the specific characteristics of our study site, such as the fully vegetated land cover, made it easier to landslide detection using only spectral information.

Based on our results, the topographic factors did not extremely contribute to higher accuracies comparing with optical data in the EQIL detection. However, several landslide areas were detected by using topographical factors, which were impossible



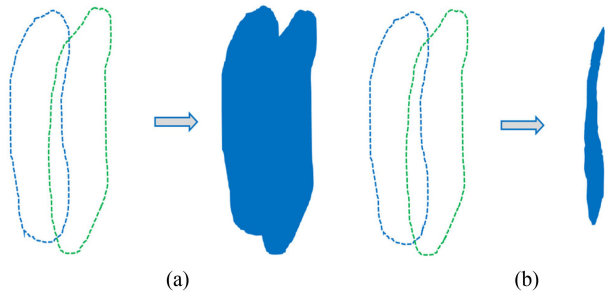


Fig. 7. Illustration of the (a) area of union and that of the and (b) overlap.

TABLE I  
RESULTING TP, FP, AND FN AREAS

Method	TP (ha)	FP (ha)	FN (ha)
CNN <sub>32_0</sub>	322.39	298.92	78.97
CNN <sub>32_0,Slope</sub>	301.42	131.55	99.94
CNN <sub>32_0,Aspect</sub>	300.92	129.12	100.44
CNN <sub>32_0,Curvat</sub>	296.03	221.14	105.33
CNN <sub>32_0,DEM</sub>	307.39	343.81	93.97
CNN <sub>32_All</sub>	273.01	157.53	128.35
CNN <sub>32_DS mode</sub>	313.91	158.24	87.45

TABLE II  
LANDSLIDE DETECTION RESULTS FOR OUR STUDY SITE FOR THE RESULTS  
BASED ON DIFFERENT TRAINING DATASETS

Method	Precision	Recall	F-score	mIOU
CNN <sub>32_0</sub>	0.52	0.80	0.63	0.46
CNN <sub>32_0,Slope</sub>	0.70	0.75	0.72	0.56
CNN <sub>32_0,Aspect</sub>	0.59	0.75	0.66	0.49
CNN <sub>32_0,Curvat</sub>	0.57	0.73	0.64	0.47
CNN <sub>32_0,DEM</sub>	0.47	0.76	0.58	0.41
CNN <sub>32_All</sub>	0.57	0.73	0.64	0.47
CNN <sub>32_DS mode</sub>	0.66	0.78	0.71	0.56

Accuracies are stated as precision, recall,  $F1$ -score, and mIOU.

to be identified by using only optical data. This matter is also dependent on the applied topographical factor. For example, adding the aspect layer resulted in the detection of some landslides that using the plan curvature was not successful. Therefore, all of the topographic factors could help to detect some landslide areas or increase the accuracy of the border of the EQIL area. However, they were unable to get higher accuracies because of their more amount of FPs and FNs. In this study, we used

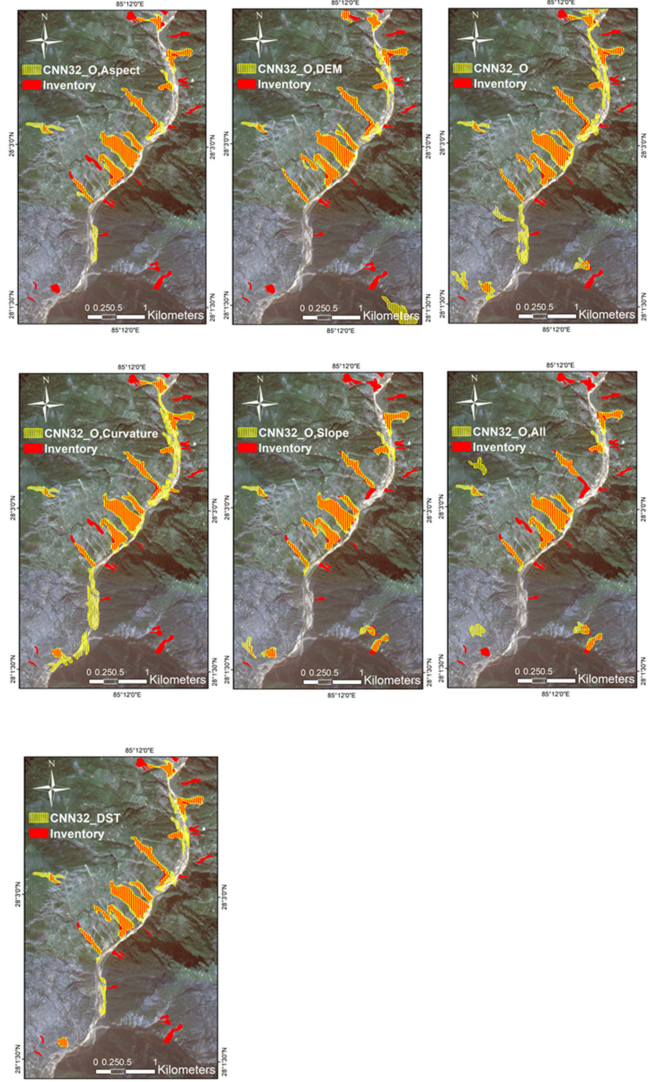
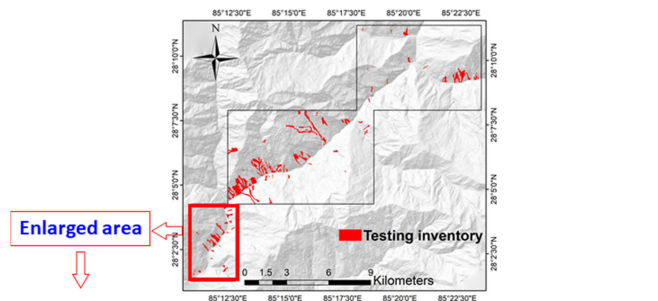


Fig. 8. Enlarged subarea of landslide detection results of the CNN model using different training datasets.

the D-S model to take advantage of all the capabilities of every applied topographic factor for landslide detection. In this regard, we integrated all the results based on all factors using the D-S model and it was helpful to merge the TPs from different results, which significantly improved the EQIL detection accuracy. The D-S model combined the majority of TPs and then allocated them to the class of the EQIL area.

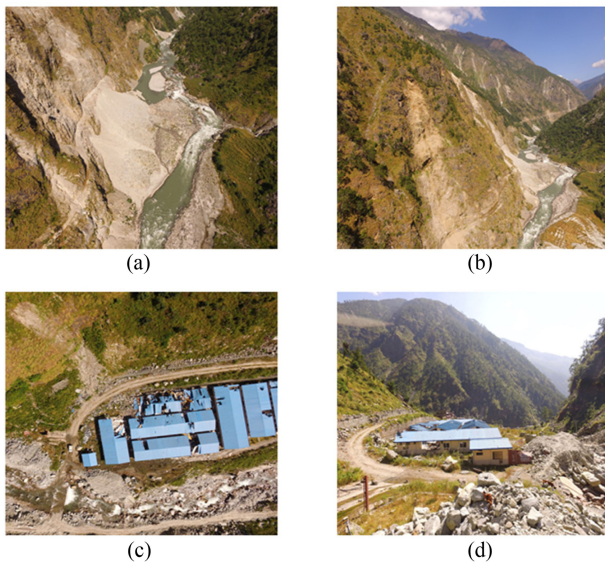


Fig. 9. (a) Landslide-induced dam near Mailung on the Trishuli river. (b) Overview of landslides coming to the riverbed. (c) Landslide debris coming to the hydroelectric project camp. (d) Damaged hydroelectric project camp near Mailung village.

## VI. CONCLUSION

Our results confirm that combining the resulting maps from two or more CNN streams is possible with the D-S model. We combined  $CNN_O$  and  $CNN_{OT}$ , which were trained by the spectral information along with different topographic factors. Thus, the role of the topographical information for landslides detection was evaluated and the accuracy metrics were calculated for any single scenario. The results were important, as landslides detection from RS data is vital for preparing reliable inventory datasets for further landslide analyses, such as susceptibility, risk modeling, and mapping. In this regard, two different training datasets were prepared using spectral and topographical information. Hence, the CNN model was trained once with only spectral information and then with both spectral and topographical ones. All trained CNN models were tested on the study site for the EQIL detection along the Trishuli river. The resulting landslide maps were validated and the model that trained with only spectral information represented a slightly better accuracy in landslide detection. The application of the D-S model to integrate all resulting maps could increase the accuracy of landslide detection. Based on the achieved results in our study, employing the CNN model along with the D-S model gives us a comprehensive view of the effect of each and all topographic factors on landslide detection. Turning to the topographic factors, the slope information could effectively remove the riverbeds, which have almost a similar spectral information from the detected EQILs.

In this study, we used the CNN model that we structured for our specific use case. Thus, the main limitation of this study can be the absence of the comparison of our results with the results of the current-designed CNNs. Our future work will focus on the application of the current-designed CNN models for our aim of the landslide detection.

## REFERENCES

- [1] H. Tanyaş *et al.*, "Presentation and analysis of a worldwide database of earthquake-induced landslide inventories," *J. Geophys. Res., Earth Surf.*, vol. 122, no. 10, pp. 1991–2015, 2017.
- [2] K. D. Marano, D. J. Wald, and T. I. Allen, "Global earthquake casualties due to secondary effects: A quantitative analysis for improving rapid loss analyses," *Nat. Hazards*, vol. 52, no. 2, pp. 319–328, Feb. 2010.
- [3] D. Petley, "Global patterns of loss of life from landslides," *Geology*, vol. 40, no. 10, pp. 927–930, 2012.
- [4] X. Fan *et al.*, "Coseismic landslides triggered by the 8th August 2017  $M_s$  7.0 Jiuzhaigou earthquake (Sichuan, China): Factors controlling their spatial distribution and implications for the seismogenic blind fault identification," *Landslides*, vol. 15, no. 5, pp. 967–983, 2018.
- [5] H. R. Pourghasemi, A. Gayen, S. Park, C.-W. Lee, and S. Lee, "Assessment of landslide-prone areas and their zonation using logistic regression, logitboost, and naïve Bayes machine-learning algorithms," *Sustainability*, vol. 10, no. 10, 2018, Art. no. 3697.
- [6] H. R. Pourghasemi, H. R. Moradi, S. M. F. Aghda, C. Gokceoglu, and B. Pradhan, "GIS-based landslide susceptibility mapping with probabilistic likelihood ratio and spatial multi-criteria evaluation models (North of Tehran, Iran)," *Arabian J. Geosci.*, vol. 7, no. 5, pp. 1857–1878, 2014.
- [7] G. Domènech *et al.*, "Modelling the role of material depletion, grain coarsening and revegetation in debris flow occurrences after the 2008 Wenchuan earthquake," *Eng. Geol.*, vol. 250, pp. 34–44, 2019.
- [8] X. Fan *et al.*, "Earthquake-induced chains of geologic hazards: Patterns, mechanisms, and impacts," *Rev. Geophys.*, vol. 57, no. 2, pp. 421–503, 2019, doi: [10.1029/2018rg000626](https://doi.org/10.1029/2018rg000626).
- [9] H. R. Pourghasemi and N. Kerle, "Random forests and evidential belief function-based landslide susceptibility assessment in western Mazandaran province, Iran," *Environ. Earth Sci.*, vol. 75, no. 3, 2016, Art. no. 185.
- [10] S. L. Chatteraj, P. K. C. Ray, and S. Kannaujia, "Simulation outputs of major debris flows in garhwal Himalaya: A geotechnical modeling approach for hazard mitigation," in *Remote Sensing of Northwest Himalayan Ecosystems*. Berlin, Germany: Springer, 2019, pp. 37–56.
- [11] S. R. Meena, O. Ghorbanzadeh, and T. Blaschke, "A comparative study of statistics-based landslide susceptibility models: A case study of the region affected by the Gorkha earthquake in Nepal," *ISPRS Int. J. Geoinf.*, vol. 8, no. 2, pp. 1–23, 2019.
- [12] O. Ghorbanzadeh, T. Blaschke, K. Gholamnia, S. R. Meena, D. Tiede, and J. Aryal, "Evaluation of different machine learning methods and deep-learning convolutional neural networks for landslide detection," *Remote Sens.*, vol. 11, no. 2, 2019. [Online]. Available: <http://www.mdpi.com/2072-4292/11/2/196>
- [13] S. T. Piralilou *et al.*, "Landslide detection using multi-scale image segmentation and different machine learning models in the higher himalayas," *Remote Sens.*, vol. 11, no. 21, 2019. [Online]. Available: <https://www.mdpi.com/2072-4292/11/21/2575>
- [14] O. Ghorbanzadeh and T. Blaschke, "Optimizing sample patches selection of CNN to improve the mIOU on landslide detection," in *Proc. 5th Int. Conf. Geographical Inf. Syst. Theory, Appl. Manage: GISTAM*, vol. 1, pp. 33–40, 2019, doi: [10.5220/0007675300330040](https://doi.org/10.5220/0007675300330040).
- [15] D. T. Bui *et al.*, "A novel ensemble artificial intelligence approach for gully erosion mapping in a semi-arid watershed (Iran)," *Sensors*, vol. 19, no. 11, 2019, Art. no. 2444.
- [16] A. Jaafari, E. K. Zenner, M. Panahi, and H. Shahabi, "Hybrid artificial intelligence models based on a neuro-fuzzy system and metaheuristic optimization algorithms for spatial prediction of wildfire probability," *Agricultural Forest Meteorol.*, vol. 266/267, pp. 198–207, 2019.
- [17] A.-L. Argentin, G. Prasicsek, J. Robl, D. Hölbling, and B. Friedl, "Detecting landslide-induced paleolakes and their impact on river course," *Geophys. Res. Abstr.*, vol. 20, 2018, Art. no. 6349.
- [18] V. Svalova, "Landslide risk management for urbanized territories," in *Risk Management Treatise for Engineering Practitioners*. London, U.K.: IntechOpen, 2019, pp. 1–19.
- [19] O. Ghorbanzadeh *et al.*, "Spatial prediction of wildfire susceptibility using field survey GPS data and machine learning approaches," *Fire*, vol. 2, no. 3, 2019. [Online]. Available: <https://www.mdpi.com/2571-6255/2/3/43>
- [20] T. G. Nachappa, S. T. Piralilou, O. Ghorbanzadeh, H. Shahabi, and T. Blaschke, "Landslide susceptibility mapping for Austria using geons and optimization with the Dempster-Shafer theory," *Appl. Sci.*, vol. 9, no. 24, 2019, Art. no. 5393.
- [21] B. T. Pham *et al.*, "A comparison of support vector machines and Bayesian algorithms for landslide susceptibility modeling," *Geocarto Int.*, vol. 34, pp. 1385–1407, 2018.

- [22] W. Chen *et al.*, "Landslide susceptibility modeling based on GIS and novel bagging-based kernel logistic regression," *Appl. Sci.*, vol. 8, no. 12, 2018. [Online]. Available: <https://www.mdpi.com/2076-3417/8/12/2540>
- [23] Z. Y. Lv, T. F. Liu, P. Zhang, J. A. Benediktsson, T. Lei, and X. Zhang, "Novel adaptive histogram trend similarity approach for land cover change detection by using bitemporal very-high-resolution remote sensing images," *IEEE Trans. Geosci. Remote Sens.*, vol. 57, no. 12, pp. 9554–9574, Dec. 2019.
- [24] M. R. Mezaal, B. Pradhan, and H. M. Rizzei, "Improving landslide detection from airborne laser scanning data using optimized Dempster–Shafer," *Remote Sens.*, vol. 10, no. 7, 2018, Art. no. 1029.
- [25] G. Danneels, E. Pirard, and H.-B. Havenith, "Automatic landslide detection from remote sensing images using supervised classification methods," in *Proc. IEEE Int. Geosci. Remote Sens. Symp.*, 2007, pp. 3014–3017.
- [26] Q. Zhu, L. Chen, H. Hu, S. Pirasteh, H. Li, and X. Xie, "Unsupervised feature learning to improve transferability of landslide susceptibility representations," *IEEE J. Sel. Topics Appl. Earth Observ. Remote Sens.*, vol. 13, pp. 3971–3930, 2020.
- [27] T. R. Martha, N. Kerle, V. Jetten, C. J. van Westen, and K. V. Kumar, "Characterising spectral, spatial and morphometric properties of landslides for semi-automatic detection using object-oriented methods," *Geomorphology*, vol. 116, no. 1/2, pp. 24–36, 2010.
- [28] D. Hölbling, P. Füreder, F. Antolini, F. Cigna, N. Casagli, and S. Lang, "A semi-automated object-based approach for landslide detection validated by persistent scatterer interferometry measures and landslide inventories," *Remote Sens.*, vol. 4, no. 5, pp. 1310–1336, 2012.
- [29] E. R. DeLancey, J. F. Simms, M. Mahdianpari, B. Brisco, C. Mahoney, and J. Kariyeva, "Comparing deep learning and shallow learning for large-scale wetland classification in Alberta, Canada," *Remote Sens.*, vol. 12, no. 1, pp. 1–20, 2020.
- [30] C. Ye *et al.*, "Landslide detection of hyperspectral remote sensing data based on deep learning with constrains," *IEEE J. Sel. Topics Appl. Earth Observ. Remote Sens.*, vol. 12, no. 12, pp. 5047–5060, Dec. 2019.
- [31] E. Guirado, S. Tabik, D. Alcaraz-Segura, J. Cabello, and F. Herrera, "Deep-learning convolutional neural networks for scattered shrub detection with google earth imagery," 2017, *arXiv:1706.00917*.
- [32] Z. Lv, T. Liu, and J. A. Benediktsson, "Object-oriented key point vector distance for binary land cover change detection using VHR remote sensing images," *IEEE Trans. Geosci. Remote Sens.*, vol. 58, no. 9, pp. 6524–6533, Sep. 2020.
- [33] O. Ghorbanzadeh, D. Tiede, Z. Dabiri, M. Sudmanns, and S. Lang, "Dwelling extraction in refugee camps using CNN-First experiences and lessons learnt," *Int. Arch. Photogrammetry, Remote Sens. Spatial Inf. Sci.*, vol. 42, no. 1, pp. 161–166, 2018.
- [34] J. A. Quinn, M. M. Nyhan, C. Navarro, D. Coluccia, L. Bromley, and M. Luengo-Oroz, "Humanitarian applications of machine learning with remote-sensing data: Review and case study in refugee settlement mapping," *Philos. Trans. Roy. Soc. A, Math., Phys. Eng. Sci.*, vol. 376, no. 2128, 2018, Art. no. 20170363.
- [35] M. Sheykhmousa, M. Mahdianpari, H. Ghanbari, F. Mohammadimanesh, P. Ghamisi, and S. Homayouni, "Support vector machine versus random forest for remote sensing image classification: A meta-analysis and systematic review," *IEEE J. Sel. Topics Appl. Earth Observ. Remote Sens.*, vol. 13, pp. 6308–6325, Sep. 2020.
- [36] Y. Lu, D. Perez, M. Dao, C. Kwan, and J. Li, "Deep learning with synthetic hyperspectral images for improved soil detection in multispectral imagery," in *Proc. 9th IEEE Annu. Ubiquitous Comput., Electron. Mobile Commun. Conf.*, 2018, pp. 666–672.
- [37] O. F. Althwaynee, B. Pradhan, and S. Lee, "Application of an evidential belief function model in landslide susceptibility mapping," *Comput. Geosci.*, vol. 44, pp. 120–135, 2012.
- [38] W. Schwanghart, M. Ryan, and O. Korup, "Topographic and seismic constraints on the vulnerability of himalayan hydropower," *Geophys. Res. Lett.*, vol. 45, no. 17, pp. 8985–8992, 2018.
- [39] "Planet application program interface: In space for life on earth," Planet-Team, 2018. [Online]. Available: <https://api.planet.com>
- [40] M. W. Moine, A. Puiissant, and J.-P. Malet, "Detection of landslides from aerial and satellite images with a semi-automatic method. Application to the Barcelonnette basin (Alpes-de-Hautes-Provence, France)," in *Proc. Landslide Process. Geomorpholog. Mapping Dyn. Model.*, 2009, pp. 1–7.
- [41] J. V. Fayne, A. Ahamed, J. Roberts-Pierel, A. C. Rumsey, and D. Kirschbaum, "Automated satellite-based landslide identification product for Nepal," *Earth Interact.*, vol. 23, no. 3, pp. 1–21, 2019.
- [42] B. Kalantar, N. Ueda, V. Saeidi, K. Ahmadi, A. A. Halin, and F. Shabani, "Landslide susceptibility mapping: Machine and ensemble learning based on remote sensing big data," *Remote Sens.*, vol. 12, no. 11, 2020, Art. no. 1737.
- [43] H. A. H. Al-Najjar, B. Kalantar, B. Pradhan, and V. Saeidi, "Conditioning factor determination for mapping and prediction of landslide susceptibility using machine learning algorithms," *Proc. SPIE*, vol. 11156, 2019, Art. no. 111560K.
- [44] M. I. Sameen and B. Pradhan, "Landslide detection using residual networks and the fusion of spectral and topographic information," *IEEE Access*, vol. 7, pp. 114363–114373, 2019.
- [45] A.-X. Zhu *et al.*, "A similarity-based approach to sampling absence data for landslide susceptibility mapping using data-driven methods," *CATENA*, vol. 183, 2019, Art. no. 104188, doi: <https://doi.org/10.1016/j.catena.2019.104188>.
- [46] X. Fan *et al.*, "Spatio-temporal evolution of mass wasting after the 2008  $M_w$  7.9 Wenchuan earthquake revealed by a detailed multi-temporal inventory," *Landslides*, vol. 15, no. 12, pp. 2325–2341, 2018.
- [47] Y. Wang, Z. Fang, and H. Hong, "Comparison of convolutional neural networks for landslide susceptibility mapping in Yanshan county, China," *Sci. Total Environ.*, vol. 666, pp. 975–993, 2019.
- [48] Z. Lv, G. Li, Z. Jin, J. A. Benediktsson, and G. M. Foody, "Iterative training sample expansion to increase and balance the accuracy of land classification from VHR imagery," *IEEE Trans. Geosci. Remote Sens.*, 2020.
- [49] K. Lu, "Extraction of buildings from aerial images," ProQuest Dissertations Theses Global: Sci. Eng. Collection, 2018. [Online]. Available: <https://search.proquest.com/docview/2087742600?accountid=13672>
- [50] H. Lu, X. Fu, C. Liu, L.-G. Li, Y.-X. He, and N.-W. Li, "Cultivated land information extraction in UAV imagery based on deep convolutional neural network and transfer learning," *J. Mountain Sci.*, vol. 14, no. 4, pp. 731–741, 2017.
- [51] Y. LeCun and Y. Bengio, "Convolutional networks for images, speech, and time series," *Handbook Brain Theory Neural Netw.*, vol. 3361, no. 10, pp. 1–14, 1995.
- [52] W. Ng, B. Minasny, and A. McBratney, "Convolutional neural network for soil microplastic contamination screening using infrared spectroscopy," *Sci. Total Environ.*, vol. 702, 2020, Art. no. 134723.
- [53] A. P. Dempster, "Upper and lower probabilities induced by a multivalued mapping," in *Classic Works of the Dempster–Shafer Theory of Belief Functions*. Berlin, Germany: Springer, 2008, pp. 57–72.
- [54] B. Feizizadeh, T. Blaschke, and H. Nazmfar, "GIS-based ordered weighted averaging and Dempster–Shafer methods for landslide susceptibility mapping in the Urmia lake basin, Iran," *Int. J. Digit. Earth*, vol. 7, no. 8, pp. 688–708, 2014.
- [55] O. Rahmati and A. M. Melesse, "Application of Dempster–Shafer theory, spatial analysis and remote sensing for groundwater potentiality and nitrate pollution analysis in the semi-arid region of Khuzestan, Iran," *Sci. Total Environ.*, vol. 568, pp. 1110–1123, 2016.
- [56] C. González, M. Castillo, P. García-Chevesich, and J. Barrios, "Dempster-Shafer theory of evidence: A new approach to spatially model wild-fire risk potential in central Chile," *Sci. Total Environ.*, vol. 613/614, pp. 1024–1030, 2018.
- [57] P. Baraldi and E. Zio, "A comparison between probabilistic and Dempster–Shafer theory approaches to model uncertainty analysis in the performance assessment of radioactive waste repositories," *Risk Anal., Int. J.*, vol. 30, no. 7, pp. 1139–1156, 2010.
- [58] F. Rottensteiner, J. Trinder, S. Clode, and K. Kubik, "Using the Dempster–Shafer method for the fusion of LIDAR data and multi-spectral images for building detection," *Inf. Fusion*, vol. 6, no. 4, pp. 283–300, 2005.
- [59] T. G. Nachappa, S. T. Piralilou, K. Gholamnia, O. Ghorbanzadeh, O. Rahmati, and T. Blaschke, "Flood susceptibility mapping with machine learning, multi-criteria decision analysis and ensemble using dempster Shafer theory," *J. Hydrol.*, vol. 590, 2020, Art. no. 125275.
- [60] H. Kim and P. H. Swain, "Multisource data analysis in remote sensing and geographic information systems based on Shafer's theory of evidence," in *Proc. 12th Can. Symp. Remote Sens. Geosci. Remote Sens. Symp.*, 1989, pp. 829–832.
- [61] Y. Zeng, J. Zhang, and J. L. van Genderen, "Comparison and analysis of remote sensing data fusion techniques at feature and decision levels," in *Proc. ISPRS 7th Midterm Symp. Remote Sens., Pixels Process.*, 2006, pp. 1–5.
- [62] B. Maser, D. Söllinger, and A. Uhl, "PRNU-based finger vein sensor identification in the presence of presentation attack data," in *Proc. Joint ARW/OAGM Workshop*, 2019, pp. 1–8.

- [63] H. Shahabi, B. Jarhani, S. T. Piralilou, D. Chittleborough, M. Avand, and O. Ghorbanzadeh, "A semi-automated object-based gully networks detection using different machine learning models: A case study of bowen catchment, Queensland, Australia," *Sensors*, vol. 19, no. 22, 2019, Art. no. 4893.
- [64] O. Rahmati *et al.*, "Spatial modeling of snow avalanche using machine learning models and geo-environmental factors: Comparison of effectiveness in two mountain regions," *Remote Sens.*, vol. 11, no. 24, 2019, Art. no. 2995.



**Omid Ghorbanzadeh** received the B.Sc. degree in mathematics from Azarbaijan Shahid Madani University, Tabriz, Iran, in 2011, and the M.Sc. degree in remote sensing and geographic information systems from the University of Tabriz, Tabriz, Iran, in 2016, working on the optimization of knowledge-based systems for the spatial problems. He is currently working toward the Ph.D. degree in geoinformatics with the Doctoral College GIScience, University of Salzburg, Salzburg, Austria.

His current project is the semantic segmentation of remote sensing data by integrating deep learning techniques with object-based image analysis. His current research interests include geoinformatics, remote sensing, image processing, computer vision, and deep learning.

Mr. Ghorbanzadeh was a recipient of the Best Student Paper award at the GISTAM 2019 Conference.



**Sansar Raj Meena** received the B.A. (Hons.) degree in geography from the University of Delhi, New Delhi, India, in 2015, and the M.Sc. degree in applied earth sciences with specialization in natural hazards risk and engineering from the ITC Faculty of Geoinformation Science and Earth Observation, University of Twente, Enschede, The Netherlands, in 2017.

He is currently a Researcher with ITC, University of Twente, Enschede, The Netherlands, and with the Z\_GIS Department of Geoinformatics, University of Salzburg, Salzburg, Austria. He specializes in remote sensing, GIS application in natural hazards, and environmental related problems.

Mr. Meena was a recipient of the University of Twente-ITC Fellowship for M.Sc. (2015) from the University of Twente, Enschede, The Netherlands, and the National Overseas Fellowship (2018) from the Government of India for doctoral research.



**Hejar Shahabi** received the B.Sc. degree in surveying engineering focusing on landscape change detection using remote sensing data from the University College of Omran and Tosseeh, Hamadan, Iran, in 2013, and the master's degree in remote sensing and geographic information systems from the University of Tabriz, Tabriz, Iran, in 2017, working on the applications of object-based image analysis (OBIA) method in image classification and natural hazards mapping.

He is currently the Head of the GIS and Surveying group with Sotorgsaz Company, Urmia, Iran. His research interests are focused on the integration of multisensor and multitemporal remote sensing data with machine learning models for natural hazards mapping and prediction. He is also interested in the integration of OBIA with deep learning models for long-term landscape change assessment.



**Sepideh Tavakkoli Piralilou** received the B.Sc. degree in pure mathematics from Azarbaijan Shahid Madani University, Tabriz, Iran, in 2011, and the master's degree in applied mathematics from the University of Tabriz, Tabriz, Iran, in 2016, working on the differential equations. She is currently working toward the Ph.D. degree in geoinformatics with the Z\_GIS Department of Geoinformatics, University of Salzburg, Salzburg, Austria.

She is currently working on probabilistic modeling object definition and spatial scaling problems in geoinformatics. Her research interests include the Dempster-Shafer theory, multiscale image segmentation, and machine learning techniques.



**Lv Zhiyong** received the M.S. and Ph.D. degrees from the School of Remote Sensing and Information Engineering, Wuhan University, Wuhan, China, in 2008 and 2014, respectively.

He was an Engineer of surveying and was with the First Institute of Photogrammetry and Remote Sensing from 2008 to 2011. He is currently with the School of Computer Science and Engineering, Xi'an University of Technology, Xi'an, China. His research interests include multi-hyper-spectral and high-resolution remotely sensed image processing,

spatial feature extraction, neural networks, pattern recognition, deep learning, and remote sensing applications.



**Thomas Blaschke** received the M.Sc. degree in geoinformatics from the University of Salzburg, in 1992 and the Ph.D. degree in geography from the University of Salzburg, in 1995.

He is a Full Professor, the Deputy Chair of the Z\_GIS Department of Geoinformatics, and Director of the Doctoral College GIScience, University of Salzburg, Salzburg, Austria. His research interests include methodological issues of the integration of GIS, remote sensing, and image processing also with aspects of participation and human-environment interaction.

His academic record includes several temporary affiliations as a Guest Professor and Visiting Scientist in Germany, the U.K., and the USA, and 470 scientific publications. He is the author, coauthor, or editor of 16 books.

Prof. Blaschke was a recipient of numerous academic prizes and awards, including the Christian Doppler Prize 1995.